Corrosion Science 100 (2015) 332–340

Contents lists available at ScienceDirect

Corrosion Science

journal homepage: www.elsevier.com/locate/corsci

# Zr–Sn–Nb–Fe–Si–O alloy for fuel cladding candidate: Processing, microstructure, corrosion resistance and tensile behavior

Liangyu Chen[a,c], Jiuxiao Li[a], Yao Zhang[a], Lai-Chang Zhang[d], Weijie Lu[a,*], Liqiang Wang[a,*], Lefu Zhang[b], Di Zhang[a]

[a] State Key Laboratory of Metal Matrix Composites, Shanghai Jiao Tong University, Shanghai 200240, China
[b] School of Nuclear Science and Engineering, Shanghai Jiao Tong University, Shanghai 200240, China
[c] School of Material Science and Engineering, Jiangsu University of Science and Technology, Zhenjiang Jiangsu 212003, China
[d] School of Engineering, Edith Cowan University, 270 Joondalup Drive, Joondalup, Perth, WA 6027, Australia

ARTICLE INFO

*Article history:*
Received 10 April 2015
Received in revised form 2 August 2015
Accepted 3 August 2015
Available online 5 August 2015

*Keywords:*
A. Zirconium
A. Alloy
B. SEM
B. TEM
C. High temperature corrosion
C. Hydrogen absorption

ABSTRACT

A Zr–Sn–Nb–Fe–Si–O alloy was prepared and its microstructure, corrosion properties, hydrogen pick-up, and mechanical behavior were investigated and correlated. Both the conventional rolled and annealed specimens (Group A) and the second β-quenched specimens (Group B) possess proper corrosion resistance and hydrogen pick-up capability within 200 days exposure in LiOH aqueous solution, which are related to the suitable chemical composition, partial recrystallized microstructure and fine second phase particles. Group A at 380 °C has slightly larger ductility in elongation than that at room temperature, whilst the elongation of Group B at 380 °C increases nearly twice of that at room temperature.



## 1. Introduction

Because of low thermal neutron absorption cross-section, proper waterside corrosion resistance, and appropriate mechanical properties, zirconium (Zr) alloys, such as Zircaloy-2, Zircaloy-4, E635, ZIRLO, M5, HANA6, and NDA, have been successfully adopted as materials in nuclear reactors [1–8]. For example, they are the major structural materials employed within the fuelled region for all water cooled nuclear power reactors and as fuel cladding, fuel channels (boxes, wrappers), pressure tubes, and calandria tubes [1–8]. During the past several decades, great efforts have been made to further improve the corrosion resistance of zirconium alloys in order to meet the requirements for higher burn-up and longer refueling period of the fuel assemblies in nuclear reactors. It is well known that Zr–Sn–Nb alloys have much better corrosion resistance than Zircaloy-4 in both deionized water and LiOH aqueous solution [1–10]. Meanwhile, besides proper corrosion resistance, adequate mechanical properties of Zr alloys are needed for applications. Therefore, the strategies including composition optimization, alloying with other elements, and/or heat treatment procedure manipulations are often adopted to improve the corrosion and mechanical properties of zirconium alloys.

Recently, many investigators have been developing new alloy compositions or exploring new process for improving corrosion resistance and other properties of zirconium alloys. For example, alloying of less than 0.2% Cu (all compositions in wt.% throughout the paper where not specified) could significantly improve the corrosion resistance of Zr-1Nb alloy. Hong et al. [11] found that the addition of 0.1–0.2% Cu could lower the weight gain of Zircaloy-4 in pressurized water at 360 °C. Sabol et al. [12] found that a small addition of V results in the formation of intermetallic phase precipitates in zirconium alloys, which is beneficial for corrosion resistance. The addition of Mo also results in microstructural refinement, suppressing abnormal grain growth, enhancing the mechanical properties and damaging tolerance under electron irradiation [13,14]. Ge has a good semi-conductive characteristic [15] and improves the corrosion resistance of Zr alloys below the content of 0.1 wt.% [16]. Many studies have revealed that Bi addition could improve the corrosion resistance of Zr-1Nb alloys in deionized water at 360 °C under a pressure of 18.6 MPa [17] but degrade the corrosion resistance of Zircaloy-4 in superheated steam at 400 °C under a pressure of

* Corresponding author. Fax: +86 21 34202749.
*E-mail addresses:* luweijie@sjtu.edu.cn (W. Lu), wang_liqiang@sjtu.edu.cn (L. Wang).

http://dx.doi.org/10.1016/j.corsci.2015.08.005
0010-938X/

10.3 MPa [18]. The dopants have significant influence on intrinsic defects in the oxide which formed on the zirconium alloys. Y doping reduces the formation energy of oxygen vacancies and increases the activation energy of diffusion of $F^{++}$ center [19]. Nb doping causes neutral Sn defects to become negatively charged Sn defects [20]. This behavior would counteract the suppression of oxygen vacancy delivered by Nb [20]. The incorporation of oxygen vacancies can stabilize tetragonal zirconia in the oxide formed in zirconium alloys [20]. In some cases, however, this stabilization would vanish due to the variation of surroundings as corrosion is sustained. Hence, tetragonal zirconia would transform to monoclinic zirconia, which is detrimental to the corrosion performance due to its shear strain and volume expansion [21]. Furthermore, Yao et al. [22] found that β-quenched Zircaloy-4 has improved corrosion resistance in LiOH aqueous solution. However, Kim et al. [23] investigated the effect of different cooling rate on the microstructure of Zr-1.5Nb-0.4Sn-0.2Fe-0.1Cr *via* water quenching and air cooling from β-region, respectively. They found martensitic structure was formed during water quenching at a fast cooling rate whilst the Widmanstatten structure was created at a slow cooling rate. As such, the corrosion behavior was improved by applying a slow cooling rate [23]. It was concluded that a decreased supersaturated Nb content in the matrix by slow cooling from β-region improves the corrosion resistance of Zr-1.5Nb-0.4Sn-0.2Fe-0.1Cr.

Similar to Ge, Si has a good semi-conductive characteristic [24]. Si also has low thermal neutron absorption cross-section. From the Zr–Si phase diagram, the solubility of Si in α- or β-Zr is considerably low [25]. Si would easily precipitate in the form of second phase particles (SPPs) in zirconium alloys, even if a small amount of Si is added. The increase in the amount of SPPs plays an important role in leading to higher dispersion strengthening contributions. Hong et al. [25] found the precipitates in the Si-free modified Zircaloy-4 are slightly coarser than those in the Si-added specimen. It was deduced that the Si addition refines the precipitates in modified Zircaloy-4 [25]. Thinner oxide film was formed in Si-enriched steel than in Si-free steel for nuclear application in corrosion test since Si in steel could prevent the diffusion of some ions [26]. Therefore, Si might be a suitable alloying candidate for zirconium alloys in terms of corrosion and mechanical properties. However, the properties of zirconium alloys with Si addition have not yet been understood.

The aim of this study was to investigate the properties of a Zr–Sn–Nb–Fe–Si–O alloy which was prepared *via* two kinds of process procedures. To assess the corrosion resistance of the experimental alloy, autoclave tests were conducted up to 200 days. Weight gain changes were observed as a measure of the corrosion resistance. In addition, the microstructure, second phase particles (SPPs) type, hydride morphology and fracture morphology were also characterized.

## 2. Materials and methods

### 2.1. Specimens

The Zr–Sn–Nb–Fe–Si–O alloy was prepared by a sequence of three vacuum arc re-melting to obtain the chemical homogeneity of the alloying elements. Nuclear grade sponge zirconium was used for the present work, containing 0.021% Fe, 0.008% Si, 0.002% Cu and 0.007% Cr. Sn, Nb, Fe and Si powders were added in the melt and the purity of powders was greater than 99.9%. Oxygen was added in the form of $ZrO_2$. The chemical compositions of the alloys are shown in Table 1, where the contents of Sn, Fe and Nb were analyzed by inductively coupled plasma atomic emission spectrometry, whilst the content of Si was determined by molybdenum blue spectrophotometric method. The as-prepared disk-shape ingots were 50 mm thick and 120 mm in diameter. After forged at 1000 °C, the ingots were reduced to 10 mm in thickness and then were β-quenched. Thereafter, plates were decladded. Specimens were prepared *via* two kinds of process procedures. For detailed characterization, each stage of the procedures is shown in Fig. 1. Some specimens were prepared by conventional method and hot rolled to 3 mm at ~0.45 $T_m$ ($T_m$: the melt point of Zr), annealed at ~0.4 $T_m$ for 1 h, followed by cold rolling to 0.6 mm thick plates with 2 intermediate heat treatments at ~0.4 $T_m$ for 1 h. After final cold rolling, specimens were annealed at ~0.4 $T_m$ for 5 h. These specimens *via* the above mentioned processing procedures were denoted as Group A. The other specimens were treated by the other processing procedures and denoted as Group B. The processing procedures of Group B were using the second β-quenching substitute for intermediate annealing when the plates were cold rolled to 1.8 mm and underwent a final annealing at ~0.35 $T_m$ for 5 h, which were different from the processing procedures for Group A. The heat treatment of quenching process was carried out in the protection of Ar. Once heat treatment was complete, specimens were quenched in cold water within 2 s if quenching was needed.

**Table 1**
Chemical composition of the materials studied in this work (wt.%).

| Alloy | Alloying elements | | | | | | |
|---|---|---|---|---|---|---|---|
| | Zr | Sn | Fe | Nb | Cr | Si | O |
| ZrNbFeSiO | Balance | 0.51 | 0.33 | 0.40 | – | 0.021 | 0.079 |
| Zircaloy-4 | Balance | 1.25 | 0.22 | – | 0.10 | – | 0.13 |
| M5 | Balance | – | <0.03 | 0.93 | – | – | 0.11 |

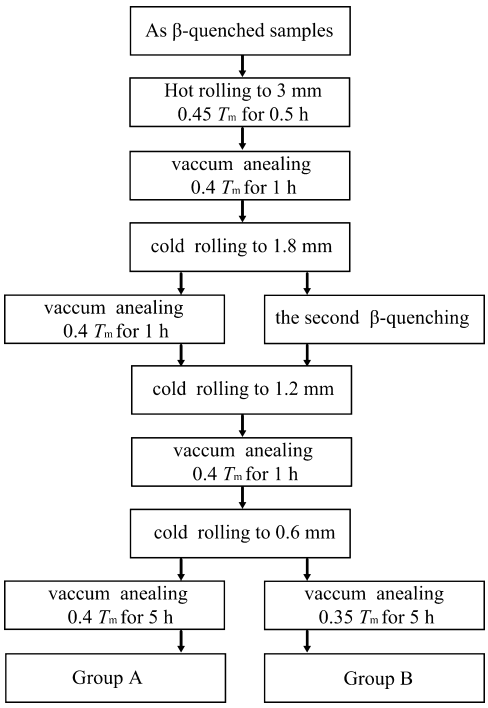


**Fig. 1.** Process flow for the experimental alloy. Regular cold work and heat treatment were adopted for Group A. However, second β-quenching and a low temperature final annealing were substituted for intermediate annealing after first cold rolling for Group B. $T_m$ is the melt point of Zr.

### 2.2. Microstructure analysis

The microstructural features of the specimens for both groups were characterized using a field emission gun scanning electron microscope (FEI Sirion 200) and a transmission electron microscope (JEOL-2100F) equipped with an energy dispersive X-ray

spectroscopy (EDS) detector with an accelerated voltage of 200 kV. The specimens for SEM observations were polished according to standard metallographic techniques and then etched in a hybrid solution composed of 10 vol.% HF, 45 vol.% $HNO_3$ and 45 vol.% $H_2O$. A gold layer sputtered to the oxide cross-sectional specimens was used to improve the surface conductivity, preventing the accumulation of electrostatic charge, thereby minimizing image artifacts. Specimens for TEM observations were prepared using a twin-jet polishing with a solution of 90 vol.% $C_2H_5OH$ and 10 vol.% $HClO_4$ at a voltage of 20 V and a temperature of −30 °C.

### 2.3. Corrosion tests

Specimens for corrosion testing were 15 mm × 20 mm in size and mechanically ground with 2000 grit SiC paper. Also, the ground specimens for the corrosion test were pickled in a solution of 30 vol.% $H_2O$, 30 vol.% $HNO_3$, 30 vol.% $H_2SO_4$, and 10 vol.% HF at temperature 30–50 °C and finally cleaned by deionized water. The corrosion resistance of the specimens was evaluated by measuring their weight gain per unit surface area in relation to the exposure time of 3, 7, 14, 42, 70, 100, 130, 160, and 200 days. The corrosion tests of stress relieved low tin Zircaloy-4 and recrystallized M5 specimens were conducted for comparison. They were obtained from China Jianzhong nuclear fuel Co., Ltd. and their chemical compositions are also shown in Table 1. According to the ASTM-G2/88 (Standard Test Method for Corrosion Testing of Products of Zirconium, Hafnium, and their alloys in water at 680 °F or in steam at 750 °F) [4], the corrosion tests were conducted with a static autoclave in deionized water and in 0.01 mol/L lithium hydroxide (LiOH) aqueous solution at 360 °C under a pressure of 18.6 MPa, respectively. Multiple specimens from each alloy were corrosion tested simultaneously in a single autoclave. The weight gain was averaged from five specimens.

### 2.4. Tensile tests

Tensile tests were performed at room temperature and 380 °C using a universal testing machine (Zwick Z100/SN3A). Dog-bone flat tensile specimens with a nominal gauge length of 15 mm and a cross-section of 12 mm × 0.6 mm were cut by electric discharge machining from the final specimens parallel to the rolling direction. The specimens were subsequently mechanically ground with 2000 grit SiC paper. A displacement rate of 1 mm/min was used for all the tests.

### 2.5. Hydrogen pick-up characterization

The distribution of hydrides on the mounted corroded specimens was revealed by etching the polished specimens with a 10 vol.% HF, 45 vol.% $HNO_3$ and 45 vol.% $H_2O$ solution. The specimens were examined with the optical microscope (Axio Imager A1 m).

Global hydrogen analysis was performed on experimental specimens of about 1 g (including the oxide layer), with hot gas extraction, followed by mass spectrometry. The extraction was realized in a high frequency furnace, the heating being maintained at 1200 °C during 30 min. The gas released was extracted with a mercury pump.

## 3. Results and discussion

### 3.1. Microstructure of alloys

Fig. 2 presents the microstructure of the experimental alloys. As shown in Fig. 2(a) the microstructure of Group A sample is composed of nearly equiaxed grains with grain size of about 1–3 μm in diameter. Precipitates are randomly distributed within the grains and along grain boundaries (although the grain boundaries are not very clear). The morphology of grains illustrates that equilibrium recrystallization was not yet reached in Group A during processing. As shown in Fig. 2(b), equiaxed grains are not observed and lath structures still exists in some regions in Group B. A large number of SPPs are interspersed along the laths. The microstructure of Group B seems far from equilibrium recrystallization. This result is mainly attributed to the second β-quenching and relatively low final annealing temperature. In addition, it could be found that the SPPs in Group B (~40 nm) are slightly smaller than those in Group A (~55 nm).

**Table 2**
Chemical composition of the second phase particles (wt.%).

| | Zr | Nb | Fe | Si |
|---|---|---|---|---|
| Group A | Bal. | 10.0–18.1 | 15.6–23.7 | 0–2.0 |
| Group B | Bal. | 9.8–17.9 | 15.8–22.8 | 0–2.0 |

Fig. 3 shows the TEM images of both groups. Two types of SPPs are presented in both experimental alloys. Both intermetallic $(Zr, Fe)_2Nb$ (Fig. 3(a)) and $(Zr, Fe, Si)_2Nb$ (Fig. 3(b)) precipitates have a face-centered cubic (FCC) structure and similar morphology. The chemical compositions of the SPPs by EDS are listed in Table 2. Actually, the structure of SPPs is strongly dependent on the chemical composition of the SPPs and the alloy [27–31]. The ratio of Fe/Nb (in wt.%) also has significant influence on the structure of SPPs in Zr-Nb-Fe system alloys. FCC SPPs are always observed in the alloys with high ratio of Fe/Nb (in wt.%) [28,31]. However, the content of Si in $(Zr, Fe, Si)_2Nb$ precipitate is less than 2% in all investigated SPPs analyzed by EDS. Supersaturated alloying elements are considered to form precipitates during heat treatment. Si is hardly soluble in β- or α-Zr [25]. It was reported that Si plays a role in phase nucleation during heat treatment and refinement of precipitates in zirconium [25]. By analyzing hundreds of SPPs, the average diameter of SPPs in Group A and Group B is 55 nm and 40 nm, respectively. The SPPs shown in Fig. 3 are the relatively big ones for sake of obtaining the diffraction patterns.

The structure in submicron scale is found in both groups of specimens because of partial recrystallization. In Group A, sub-grains with grain size less than 200 nm in diameter are found (Fig. 3(c)). It is deduced that grains observed in Fig. 2(a) consist of several sub-grains. In Group B (Fig. 3(d)), lath structures associated with the second β-quenching is preserved after final annealing. The width of laths is about 200 nm. So far, it is believed that the alloys with refined grains extend the steady state of oxidation at a low temperature (such as the temperature of corrosion test in this study) [32,33]. The reason accounting for this phenomenon is that protective oxide film forming on grain boundaries or other interfaces can maintain the steady state of oxidation and prevent $O^{2-}$ from ingressing the interior of grains [32]. Zhang et al. [33] constructed a computation model of corrosion rate *versus* grain size of nanocrystalline zirconium and their calculated results showed that nanocrystalline zirconium has improved corrosion resistance than the zirconium alloys with coarse grain size.

### 3.2. Corrosion tests and oxide cross-sectional microstructure

Fig. 4 displays the corrosion weight gain as a function of exposure time after the autoclave tests. The weight gains of Group A and Group B are lower than those of Zircaloy-4 and M5 after 200 days exposure in both conditions. The weight gains of Zircaloy-4 in current work are close to that in Ref. [34]. All specimens reveal protective uniform oxide behavior in the beginning of the tests. A relatively rapid increase of weight gain is observed in Zircaloy-4 in deionized water and in LiOH aqueous solution, after 100 days and

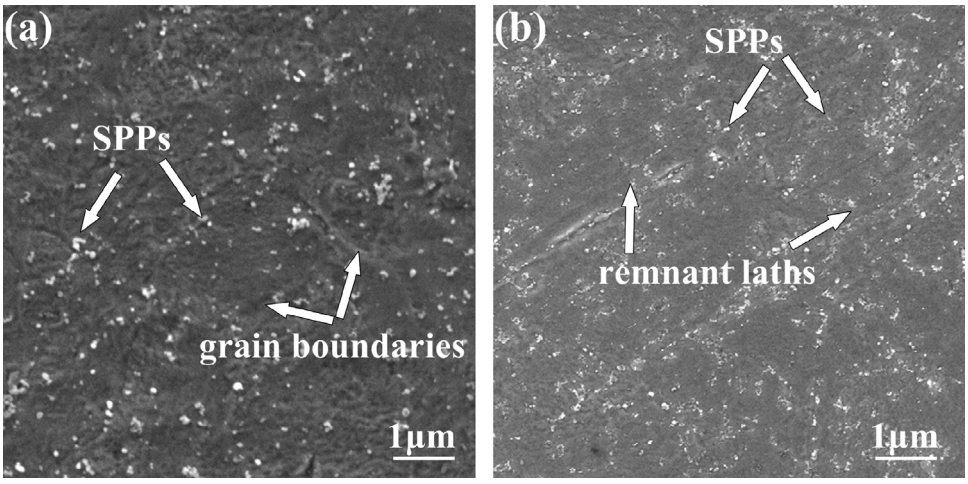


**Fig. 2.** SEM images showing characteristic microstructures of experimental alloys: (a) Group A, and (b) Group B. Equiaxed grains microstructure with evenly distributed second phase particles (SPPs) was found in Group A. Partial microstructure with remnant lath structure in some regions was found in Group B, of which SPPs are relative smaller than those in Group A.

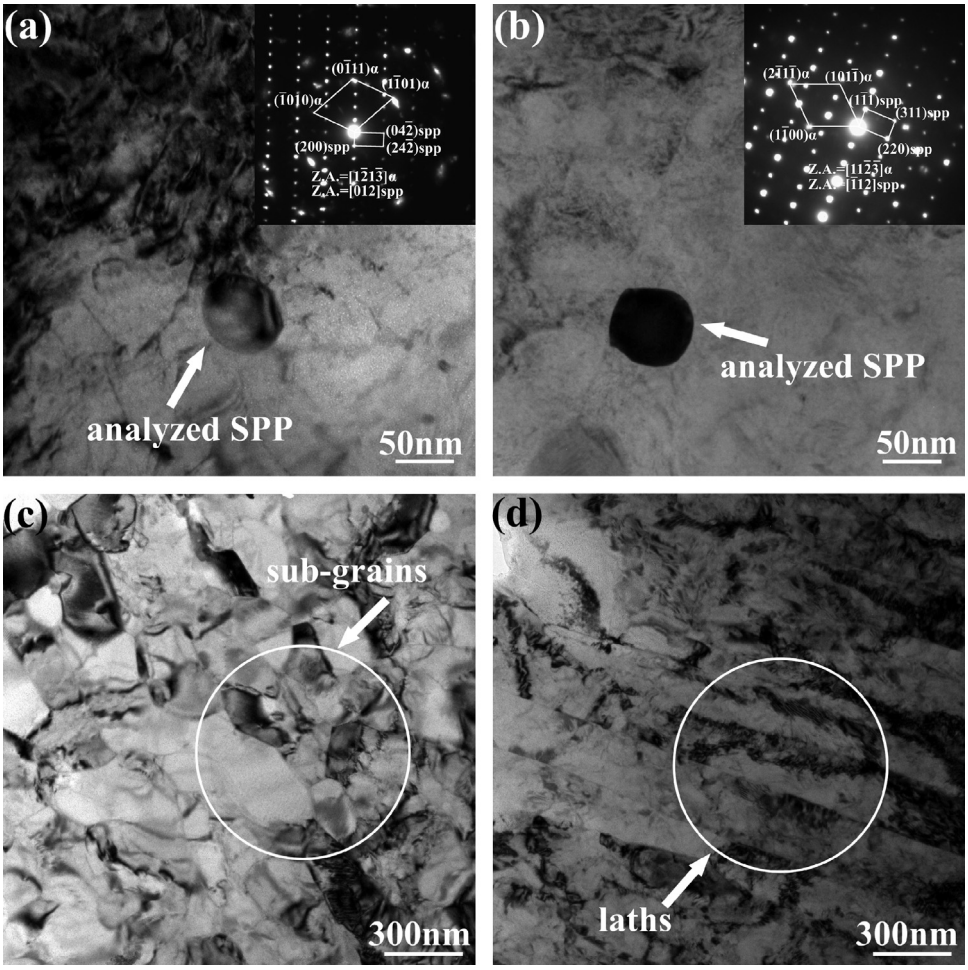


**Fig. 3.** TEM images of SPPs in: (a) Group A and (b) Group B. The insets show the selected area diffraction patterns of the precipitates. (c) Sub-grains in some regions in Group A, with grain size of about or less than 200 nm. (d) Lath structure preserved after final annealing in Group B. SPPs: second phase particles.

70 days, respectively. After 200 days exposure, both experimental alloy have quite a low weight gain and do not show an abrupt transition into an accelerated rate in deionized water (Fig. 4(a)). In LiOH aqueous solution, Group A exhibits typical corrosion kinetics with an indication of change from pre- to post-transition at around 160 days as same as M5, and Group B is still in pre-transition after 200 days exposure (Fig. 4(b)). The corrosion resistance depends significantly on the corrosion transition point. Higher corrosion resistance is related to a longer pre-transition period [6].

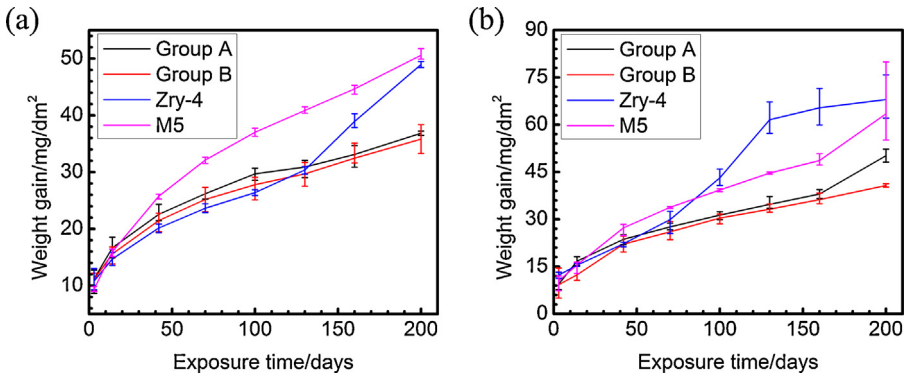


**Fig. 4.** Corrosion weight gain *versus* exposure time of all specimens in: (a) deionized water, and (b) in 0.01 mol/L LiOH aqueous solution at 360 °C/18.6 MPa. In deionized water condition, none of specimens showed post-transition phenomenon except Zircaloy-4 during corrosion test. In LiOH aqueous solution condition, nevertheless, all specimens show post-transition phenomenon except Group B specimens before 200 days exposure time.

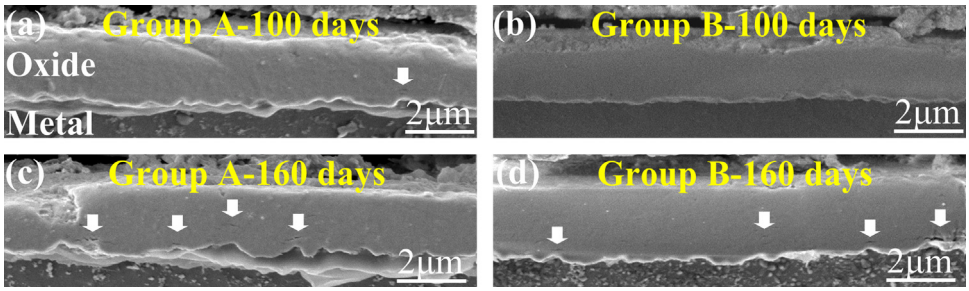


**Fig. 5.** SEM micrographs representative of the oxide (cross-section) in LiOH aqueous solution condition: (a) Group A after 100 days exposure, (b) Group A after 160 days exposure, (c) Group B after 100 days exposure and (d) Group B after 160 days exposure. More cracks and sharper undulations are found in Group A compared to Group B.

Fig. 5 shows the cross-sectional microstructure of the oxide at 100 days and 160 days in LiOH aqueous solution. A continuous oxide layer (~2 μm) has been observed for both groups (Fig. 5(a) and (b)) at 100 days exposure. It is evident that few visible cracks are presented on the oxide. This finding indicates that the oxides formed on both group specimens have strong protectiveness against the oxidants access to the metal [6,9]. However, the undulations of interface of oxide/metal in Group A are slightly sharper than those in Group B. It is important to note that the cracks paralleling to the interface are suggested relating to the transition in oxidation kinetics and have been associated with the undulations of interface [2,35,36]. The cracks are always presented in the oxide when the undulations become sharp [2,6,35,36]. This means that the oxide with mild undulations would have fewer cracks and stronger protectiveness. When the exposure time is increased to 160 days, the thickness of oxides on both groups has a small amount of growth (Fig. 5(c) and (d)). The spalling presented in Fig. 5(c) on the left of oxide might be artificial during specimen preparation. The undulations of interface of oxide/metal in Group A get sharper than those at 100 days. Lots of cracks are visible above the crests of undulations of Group A and parallel to the interface (Fig. 5(c)). It should be noted that 160 days exposure time is critical point of from pre- to post-transition for Group A (Fig. 4(b)). These cracks are suggestive of the closing corrosion kinetic transition [2]. By comparison, the undulations in Group B are much milder than those in Group A and the cracks in the oxide of Group B are correspondingly smaller (Fig. 5(d)). This observation is in good agreement with the corrosion result of Group B in (Fig. 4(b)).

Optimizing chemical composition of zirconium alloys is one of relevant factors for improving corrosion resistance. The composition of experimental alloy is still according to Hauffe–Wagner theory [15]. Sn is originally added to mitigate the deleterious effects of nitrogen in deteriorating the corrosion resistance. Nevertheless, Sn may contribute to the stabilization of the tetragonal phase which was suggested by Wei et al. [37]. A recent work performed by Bell et al. [20] suggests that Sn may cancel out the suppression of oxygen vacancy by Nb. The tetragonal phase in the oxide can be stabilized by the incorporation of oxygen vacancies [20]. Thus, the increased concentration of oxygen vacancy contributes to the increased amount of tetragonal phase. Since nitrogen is better controlled by developed melting and processing technology, Sn is reduced to 0.4–0.5% in this work.

On the basis of providing precipitates of the intermetallic phase, Fe and Nb are added in alloys. Fe is a traditional alloying element added in Zr alloys to enhance corrosion resistance. In α-phase, its solubility is very low in the region of 120 ppm at the maximum solubility temperature [38]. Therefore, Fe would easily precipitate during heat treatment. According to the Zr–Nb binary phase diagram [39], a monotectoid transformation occurs at about 600 °C. Hence, the heat treatment temperature was controlled below 600 °C (0.4 $T_m$ ~577 °C) in order to eliminate the formation of β-Zr which plays a detrimental role in forming oxide film [40]. Meanwhile, high content Nb in matrix is also harmful to corrosion resistance [4]. As the addition of 0.38% Nb in the alloy is close to its solid solubility limit in α-Zr, partial amount of Nb would precipitate during annealing as SPPs.

Si was little reported as an alloying element in previous studies [25]. It was reported that Si addition results in a refinement of precipitate and plays an important role in phase nucleation during heat treatment [25]. Furthermore, it is well known that the corrosion of zirconium alloys takes place at the oxide/metal interface. The Si-containing SPPs is incorporated into oxide during corrosion. Si would turn to $Si^{4+}$ when oxygen partial pressure is high enough. The highest oxidation valence state of Si is +4. The valence of Zr is 4+ in $ZrO_2$, equal to that of $Si^{4+}$. According to Hauffe–Wagner theory [15], $Si^{4+}$ could keep the local electrical neutrality in oxide and would not produce oxygen vacancies. However, the effect of Si in the oxide may be much more complicated than that we expected in corro-

sion. There are lots of intrinsic point defects existing in zirconia, such as vacancies and interstitial atoms [41]. Both experiments and calculations through density function theory have demonstrated that charged oxygen vacancies in zirconia can trap electrons from Si to form F centers (neutral oxygen vacancies) [41]. The reason is that the band gap of Si is smaller than that of monoclinic zirconia and oxygen vacancies can trap electrons from the conduction band of Si [42]. Therefore, a plausible mechanism for the effect of Si on corrosion resistance is suggested as followed. The charged oxygen vacancies become uncharged by trapping electrons from Si. As the activation energy of diffusion for uncharged vacancies is much higher than that of charged vacancies [19], the mobility of vacancies decrease. As known, ion conductivity in zirconia is mediated *via* oxygen vacancies [19]. The decrease in the mobility of vacancies can reduce the mobility of oxygen ions to some extent. For this reason, the corrosion resistance could be improved.

The distinct corrosion resistance between Group A and Group B is related to the difference in microstructure. The degree of recrystallization of Group B is lower than that of Group A. Park et al. [6] discussed the effect of the alloy microstructure on corrosion and concluded that the oxides growing at an expense of the partially recrystallized microstructure have larger columnar grains when compared to that of the fully recrystallized one. On the other hand, the size of SPPs in Group B is smaller than that in Group A. Many studies [5,21,43] show that the size of SPPs should be controlled in a suitable range in order to obtain better corrosion resistance of zirconium alloys, since large oxidized SPPs are apt to promote a cracking nearby, leading to an increase in corrosion rate. Thus, these reasons for Group B might be the main factors contributing to better corrosion resistance compared to Group A in LiOH aqueous solution within 200 days exposure.

### 3.3. Hydrogen pick-up and the morphology of hydrides

A large amount of hydrogen absorbed by Zr alloys in nuclear reactors has become one of the factors limiting the achievable lifetime for fuel because of the concern that such areas might be very brittle [44]. The global hydrogen content measurement of experimental alloys at the exposure time of 200 days was performed by hot gas vacuum extraction. Table 3 shows the hydrogen uptake and the calculated hydrogen pick-up fraction for each specimen at 200 days exposure in LiOH aqueous solution. For the low content obtained on all specimens, the uncertainty is lower than 10%. The experimental alloys have lower hydrogen uptake under this corrosion condition after 200 days exposure. Moreover, under the corrosion condition and tested time used in this work, the hydrogen pick-up fraction of Group A is slightly higher than that of M5 and Group B has similar hydrogen pick-up fraction as M5. Indeed, it has been reported that the hydrogen content increases and the corrosion rate decreases with the corrosion time [45]. The hydrogen pick-up fraction with the corrosion time increases before transition and drops rapidly after corrosion transition [45]. After 200 days exposure in LiOH aqueous solution, the Group B sample is still before transition and M5 is in post-transition. However, the hydrogen pick-up fractions of Group B and M5 are almost the same, implying Group B have lower hydrogen pick-up rate in LiOH aqueous solution during 200 days exposure.

**Table 3**
Hydrogen uptake and pickup fraction for each specimen after 200 days exposure in LiOH aqueous solution.

| Specimens | Hydrogen uptake (ppm) | Hydrogen pickup fraction (%) |
|---|---|---|
| Group A | 91 | 22.9 |
| Group B | 69 | 21.4 |
| Zry-4 | 186 | 43.1 |
| M5 | 107 | 21.7 |

Fig. 6 shows the cross-section of hydride morphology of both groups after 200 days exposure time in LiOH aqueous solution. After

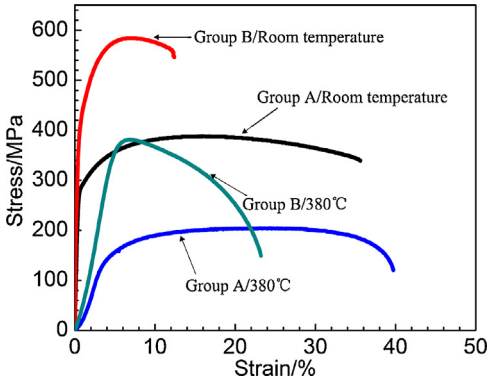


**Fig. 7.** Stress-strain curves for Group A and Group B specimens at room temperature and at 380 °C. The tensile strength reduces for both groups specimens at 380 °C. The elongation of Group A at 380 °C is only a slight greater than that at room temperature, whilst the elongation of Group B at 380 °C increases nearly twice of that at room temperature.

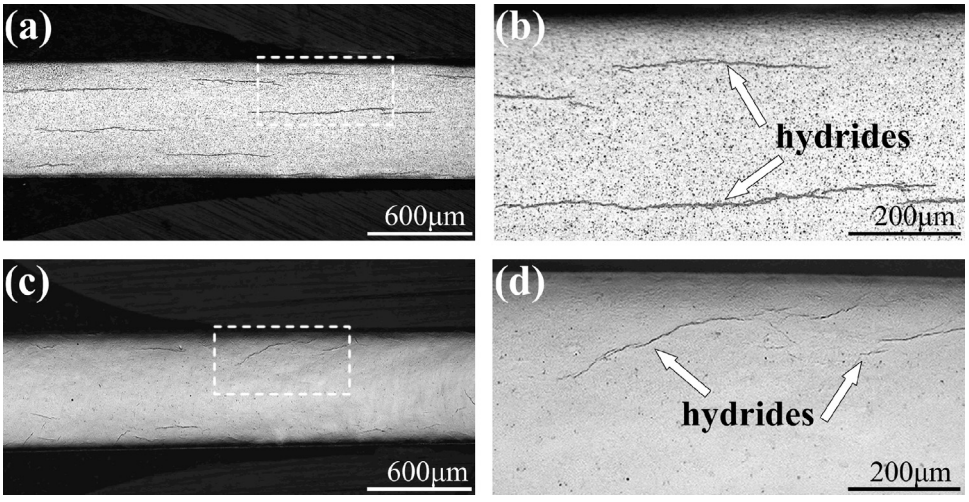


**Fig. 6.** Hydrides morphology of (a) Group A and (c) Group B. (b) and (d) show magnified micrographs for the square regions marked in (a) and (c), respectively. Large quantities of hydrides parallel to interface are found in Group A. The orientation of hydrides in Group B is random.

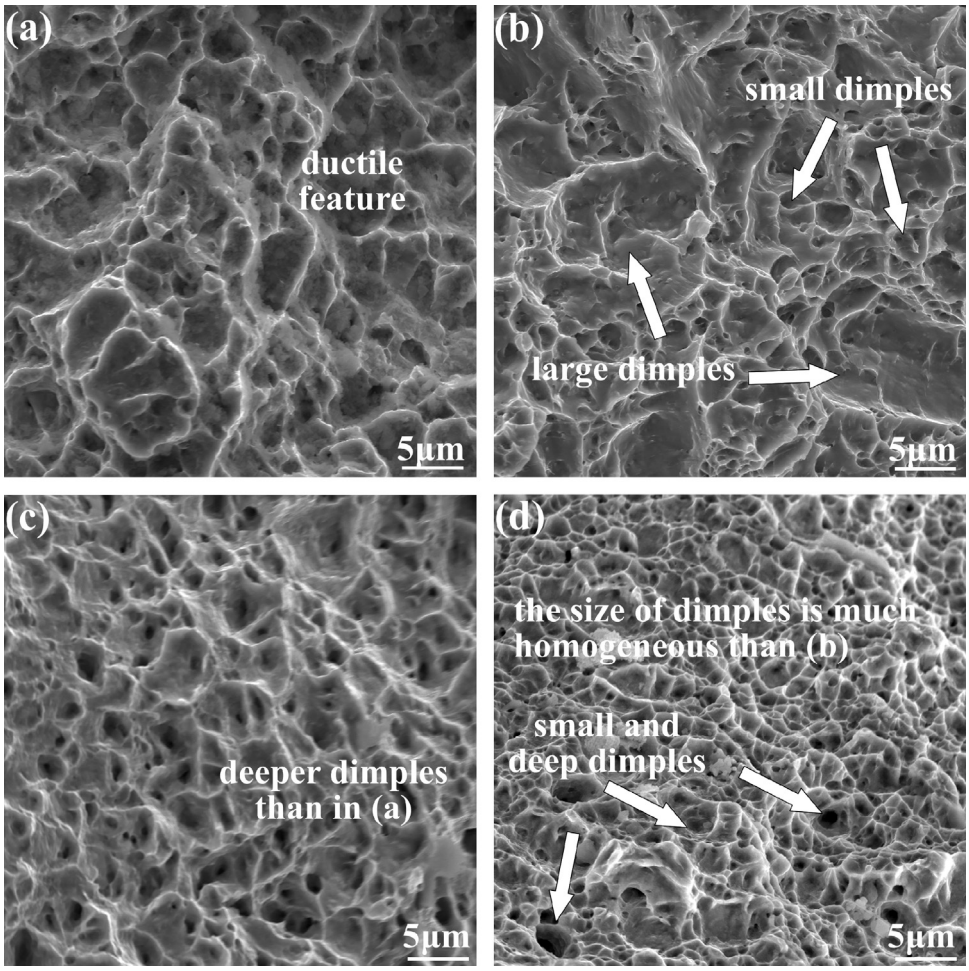


**Fig. 8.** Tensile fractographs of (a) Group A and (b) Group B specimens at room temperature, (c) Group A and (d) Group B specimens at 380 °C. Ductile dimples are predominant in the fracture surfaces of all specimens, which reveal a ductile nature for Group A and Group B specimens. The size of dimples in Group B becomes much more homogeneous at 380 °C than that at room temperature. This is the main reason contributing to the considerable enhancement of elongation for Group B at 380 °C.

corrosion test for 200 days, long hydride strings are observed in Group A and parallel to interface of oxide and metal (Fig. 6(a)). Fig. 6(b) shows a magnified micrograph for the square region marked in Fig. 6(a). The hydrides are long and thick. The hydride morphology of Group B can be seen in Fig. 6(c). The Group B have relatively clean interior, implying its low hydrogen pick-up which corresponds to corrosion resistance. Fewer hydride strings are visible and they have random orientation. Fig. 6(d) is the magnified micrograph for the square region marked in Fig. 6(c). It could be observed that the hydrides are shorter and thinner in the matrix compared to Group A, which may correspond to its low hydrogen uptake. Kumar et al. [46] reported that hydrides have a strong orientation relative to the matrix by EBSD study. Hsu et al. [44] ever studied zirconium hydride precipitates in Zircaloy-4 tubes along the circumferential direction of stress-relief anneal cladding specimens, and along or near the grain boundary of recrystallization anneal cladding specimens. Thus, the orientation of hydrides is considered to be associated with the process procedures.

Various processing procedures produce different microstructures and distributions of stresses, which result in discrepant orientation of hydrides in the matrix [47,48]. In general, the material is more prone to failure if the interlinked-structure of hydrides aligns in a direction perpendicular to interface of specimen and oxide [46]. In this case, hydrogen embrittlement takes place easily [47]. Long hydride strings are apt to make microcrack grow and provide more "shortcut" for $O^{2-}$ and $H^{+}$ to diffuse. In the present work, almost no hydrides are found in the direction perpendicular to interface in Group A. Therefore, hydrogen embrittlement is considered low in Group A. In Group B, some hydrides are in random orientation, not perpendicular or parallel to the interface; this type of hydrides may also have negative effect for corrosion behavior of the alloy. However, it is important to mention that the hydrogen uptake of Group B is considerably low. Thus, the hydrides observed in Group B are short and thin (Fig. 6c). In fact, the solubility limit of hydrogen at the working temperature is about 140 ppm for Zr alloys. The hydrogen uptake of Group B would be still below the solubility limit of hydrogen in the matrix after 200 days exposure at the working temperature. It implies that the negative effect introduced by hydrides would not be presented within 200 days tests.

### 3.4. Tensile test and morphology of fracture

Fig. 7 shows the stress-strain curves responses of various processing at room temperature and 380 °C. It could be clearly seen that both groups exhibit considerably different mechanical properties. At room temperature, the elongation and the ultimate tensile strength of Group A are about 36 % and 390 MPa, respectively. The second β-quenching in process procedure for Group B results in a large increase in yield strength and in ultimate tensile strength with a decrease in elongation. Martensitic structure is produced

during $\beta \rightarrow \alpha$ transition and large amount dislocations would be generated in $\alpha$-laths [49]. This is the main reason accounting for the discrepancy in mechanical properties between both groups. At 380 °C, the tensile strength of both group specimens decreases. The elongation of Group A increases to 40%, slightly higher than that at room temperature. However, the elongation of Group B specimens is 23.2% at 380 °C, nearly twice as that at room temperature. The explanation of such a large increase in elongation for Group B may result from dynamic recovery or dynamic recrystallization under 380 °C and the effect of an applied stress on the recrystallization of zirconium alloy [50], since Group B has a partial recrystallized microstructure. As previous reported in Ref. [51], the ultimate tensile strength of Zircaloy-4 is about 400 MPa, which is almost the same as that of Group A. However, hydrogen brittle of Zircaloy-4 would be more severe than that of Group A at the corrosion conditions and tested time in this work, as the weak corrosion resistance of Zircaloy-4.

Fig. 8 shows the fracture fractographs of the tensile specimens at both room temperature and 380 °C. Group A, which has a larger fracture strain at room temperature, displays typical ductile fracture surfaces with a lot of dimples (Fig. 8(a)). The ductility of the specimens can be attributed to the good plasticity of the specimens. The fracture surface of the Group B also consists of lots of dimples, as shown in Fig. 8(b). However, the size of dimples is much inhomogeneous. Several large dimples are associated with numerous small dimples. This inhomogeneity may result from the inhomogeneous microstructure of Group B which contains remnant laths (Fig. 2(a)). This inhomogeneity in size of dimples also leads to the lower elongation at room temperature. The similar ductile fracture surfaces are observed at 380 °C for Group A (Fig. 8(c)). The depth of the dimples in the fracture of the Group A at 380 °C is a slightly greater than that at room temperature. Therefore, the elongation of Group A increases at 380 °C. As shown in Fig. 8(d), the fracture surface of Group B is considerably different from that at room temperature and consists of a large number of small and deep dimples formed by microvoid coalescence. The size of dimples becomes homogeneous and no large dimple is observed. As mentioned above, the microstructure of Group B seems far from equilibrium recrystallization. The dynamic recovery or dynamic recrystallization would take place under the effect of elevated temperature and applied stress [50]. The microstructure of Group B would be much more homogeneous than that at room temperature. Therefore, the probability of the formation of microvoids in different areas is more or less the same during plastic deformation. Accordingly, the size of dimples is evenly distributed, thus enhancing the elongation of Group B.

## 4. Conclusion

In this work, the microstructure of experimental alloys was characterized by scanning electron microscopy and transmission electron microscopy. Meanwhile, the corrosion properties, hydrogen pick-up, and tensile behavior were also examined. Some conclusions can be drawn as follows:

1. Equiaxed grain microstructure with evenly distributed SPPs is obtained by conventional rolling and annealing process in Group A, whilst the process of Group B adopting second $\beta$-quenching and low temperature final annealing contributes to a lath reserved microstructure. The intermetallic $(Zr, Fe)_2Nb$ type and $(Zr, Fe, Si)_2Nb$ precipitates are found in both groups and both have a face-centered cubic structure. The average diameter of SPPs in Group A and Group B is 55 nm and 40 nm, respectively.
2. Both groups possess proper corrosion resistance within 200 days exposure in LiOH aqueous solution, which mainly result from their suitable chemical composition. Comparing the microstructures of Group A and Group B, partial recrystallized microstructure and fine second phase particles are beneficial for improving corrosion resistance.
3. The hydrogen pick-up of experimental alloys is low after 200 days exposure in LiOH aqueous solution. Almost no hydrides are found in the direction perpendicular to interface in Group A. In Group B, some hydrides are in random orientation. However, the hydrogen uptake of Group B is lower than that of Group A after 200 days exposure in LiOH aqueous solution.
4. The elongation of Group A at 380 °C is a slight greater than that at room temperature, whilst the elongation of Group B at 380 °C increases nearly twice of that at room temperature. Reason for large incremental elongation in Group B is its partial recrystallization microstructure occurred in dynamic recovery or dynamic recrystallization under 380 °C tensile test.

## Acknowledgments

The authors would like to acknowledge a financial support provided by 973 Program under Grant No. 2014CB046701, National Science Foundation under Grant No. 51302168. Shanghai Natural Science Foundation under Grant No. 12ZR1445500, New Teachers' Fund for Doctor Stations, Ministry of Education under Grant No. 20120073120007. The authors also would like to acknowledge Instrumental Analysis Center of Shanghai Jiao Tong University for providing technology support.

## References

[1] P.A. Burr, S.T. Murphy, S.C. Lumley, M.R. Wenman, R.W. Grimes, Hydrogen accommodation in Zr second phase particles: implications for H pick-up and hydriding of Zircaloy-2 and Zircaloy-4, Corros. Sci. 69 (2013) 1–4.
[2] V. Likhanskii, M. Kolesnik, On the evolution of wave structure at the metal/oxide interface during oxidation of Zr alloys, Corros. Sci. 87 (2014) 416–420.
[3] B. Panicaud, J.-L. Grosseau-Poussard, D. Retraint, M. Guérain, L. Li, On the mechanical effects of a nanocrystallisation treatment for $ZrO_2$ oxide films growing on a zirconium alloy, Corros. Sci. 68 (2013) 263–274.
[4] G.P. Sabol, ZIRLO™–an alloy development success, J. ASTM Int. 2.2 (2005) 3–24.
[5] P. Bossis, D. Pecheur, L. Hanifi, J. Thomazet, M. Blat, Comparison of the high burn-up corrosion on M5 and low tin Zircaloy-4, J. ASTM Int. 3 (2006) 494–525.
[6] V.V. Likhanskii, T.N. Aliev, M.Y. Kolesnik, I.A. Evdokimov, V.G. Zborovskii, Method of elastic energy minimization for evaluation of transition parameters in oxidation kinetics of Zr alloys, Corros. Sci. 61 (2012) 143–147.
[7] L. Chen, J. Li, Y. Zhang, W. Lu, L. Zhang, L. Wang, D. Zhang, Effect of low temperature pre -deformation on precipitation behavior and microstructure of a Zr–Sn–Nb–Fe–Cu–O alloys during fabrication, J. Nucl. Sci. Tech. (2005), http://dx.doi.org/10.1080/00223131.2015.1059776 (in press).
[8] W. Gong, H. Zhang, C. Wu, H. Tian, X. Wang, The role of alloying elements in the initiation of nanoscale porosity in oxide films formed on zirconium alloys, Corros. Sci. 77 (2013) 391–396.
[9] W. Gong, H. Zhang, Y. Qiao, H. Tian, X. Ni, Z. Li, et al., Grain morphology and crystal structure of pre-transition oxides formed on Zircaloy-4, Corros. Sci. 74 (2013) 323–331.
[10] T. Arima, K. Miyata, Y. Inagaki, K. Idemitsu, Oxidation properties of Zr–Nb alloys at 500–600 C under low oxygen potentials, Corros. Sci. 47 (2005) 435–446.
[11] H.S. Hong, J.S. Moon, S.J. Kim, K.S. Lee, Investigation on the oxidation characteristics of copper-added modified Zircaloy-4 alloys in pressurized water at 360 °C, J. Nucl. Mater. 297 (2001) 113–119.
[12] G.P. Sabol, R.J. Comstock, U.P. Nayak, Effect of dilute alloy additions of molybdenum, niobium, and vanadium on zirconium corrosion, Zirconium in the Nuclear Industry: 12th International Symposium ASTM STP 1354 (2000) 525–544.
[13] Y.B. Chun, S.K. Hwang, S.I. Kwun, M.H. Kim, Abnormal grain growth of Zr-1 wt.% Nb alloy and the effect of Mo addition, Scr. Mater. 40 (1999) 1165–1170.
[14] J.H. Lee, S.K. Hwang, K. Yasuda, C. Kinoshita, Effect of molybdenum on electron radiation damage of Zr-base alloys, J. Nucl. Mater. 289 (2001) 334–337.
[15] K. Hauffe, Oxidation of Metals, Plenum Press, New York, 1965.
[16] X. Xie, J. Zhang, M. Yao, B. Zhou, J. Peng, X. Liang, Oxide microstructural evolution of Zr-0.7Sn-0.35Nb-0.3Fe alloys containing Ge corroded in lithiated water, J. Nucl. Mater. 451 (2014) 255–263.

[17] L. Zhu, M.Y. Yao, G.C. Sun, W.J. Chen, J.L. Zhang, B.X. Zhou, Effect of Bi Addition on the corrosion resitance of Zr-1Nb alloy in deionized water at 360 °C and 18.6 MPa, Acta Metall. Sin. 49.1 (2013) 51–57 (in Chinese).
[18] X.F. Xie, M.Y. Yao, L.H. Zou, J.L. Zhang, J.C. Peng, B.X. Zhou, Effect of Bi addition on the corrosion resistance of Zr-4 in superheated steam at 400 °C/10.3 MPa, Acta Metall. Sin. 48 (2012) 1097–1102 (in Chinese).
[19] A. Eichler, Tetragonal Y-doped zirconia: structure and ion conductivity, Phys. Rev. B. 64 (2001) 174103.
[20] B.D.C. Bell, S.T. Murphy, P.A. Burr, R.W. Grimes, M.R. Wenman, Accommodation of tin in tetragonal $ZrO_2$, J. Appl. Phys. 117 (2015) 084901.
[21] W. Qin, C. Nam, H.L. Li, J.A. Szpunar, Tetragonal phase stability in $ZrO_2$ film formed on zirconium alloys and its effects on corrosion resistance, Acta Mater. 55 (2007) 1695–1701.
[22] M.Y. Yao, B.X. Zhou, Q. Li, W.Q. Liu, X. Geng, Y.P. Lu, A superior corrosion behavior of Zircaloy-4 in lithiated water at 360 °C/18. 6 MPa by β-quenching, J. Nucl. Mater. 374 (2008) 197–203.
[23] H.G. Kim, J.H. Baek, S.D. Kim, Y.-H. Jeong, Microstructure and corrosion characteristics of Zr-1.5Nb-0.4 Sn-0.2Fe-0.1Cr alloy with α β-annealing, J. Nucl. Mater. 372 (2008) 304–311.
[24] A.A. Arie, W. Chang, J.K. Lee, Electrochemical characteristics of semi conductive silicon anode for lithium polymer batteries, J. Electroceramics 24 (2010) 308–312.
[25] H.S. Hong, S.J. Kim, K.S. Lee, Influence of dilute silicon addition on the oxidation resistance and tensile properties of modified Zircaloy-4, J. Nucl. Mater. 304 (2002) 8–14.
[26] Y. Kurata, Corrosion behavior of Si-enriched steels for nuclear applications in liquid lead-bismuth, J. Nucl. Mater. 437 (2013) 401–408.
[27] P.A. Burr, S.T. Murphy, S.C. Lumley, M.R. Wenman, R.W. Grimes, Hydrogen solubility in zirconium intermetallic second phase particles, J. Nucl. Mater. 443 (2013) 502–506.
[28] R. Qiu, B. Luan, L. Chai, Y. Zhou, J. Chen, Review of second phase particles on zirconium alloys(II): Zr–Sn–Nb–Fe alloys, Chin. J. Nonferrous Met. 6 (2012) 1606–1615.
[29] C. Toffolon, J. Brachet, C. Servant, L. Legras, D. Charquet, P. Barberis, J. Mardon, Experimental study and preliminary thermodynamic calculations of the pseudo-ternary ZrNbFe (O, Sn) system, in: Zirconium in the Nuclear Industry, 13th Symposium, ASTM STP 1423, West Conshohocken: ASTM International, 2002, pp. 361–382.
[30] P. Barberis, D. Charquet, V. Rebeyrolle, Ternary Zr–Nb–Fe (O) system: phase diagram at 853K and corrosion behaviour in the domain Nb < 0.8%, J. Nucl. Mater. 326 (2004) 163–174.
[31] H.G. Kim, J.Y. Park, Y.H. Jeong, Ex-reactor corrosion and oxide characteristics of Zr–Nb–Fe alloys with the Nb/Fe ratio, J. Nucl. Mater. 345 (2005) 1–10.
[32] E.D. Hondros, M.P. Seah, Segregation to interfaces, Int. Met. Rev. 22 (1977) 262–301.
[33] X.Y. Zhang, M.H. Shi, C. Li, N.F. Liu, Y.M. Wei, The influence of grain size on the corrosion resistance of nanocrystalline zirconium metal, Mater. Sci. Engi. A. 448 (2007) 259–263.
[34] G.P. Sabol, R.J. Comstock, R.A. Weiner, P. Larouere, In-reactor corrosion performance of ZIRLO and Zircaloy-4, Zirconium in the Zuclear Industry: 10th International Symposium ASTM STP 1245 (1994) 724–744.
[35] N. Vermaak, G. Parry, R. Estevez, Y. Bréchet, New insight into crack formation during corrosion of zirconium-based metal-oxide systems, Acta Mater. 61 (2013) 4374–4383.
[36] N. Ni, S. Lozano-Perez, J.M. Sykes, G.D.W. Smith, C.R.M. Grovenor, Focussed ion beam sectioning for the 3D characterisation of cracking in oxide scales formed on commercial ZIRLO™ alloys during corrosion in high temperature pressurised water, Corros. Sci. 53 (2011) 4073–4083.
[37] J. Wei, P. Frankel, E. Polatidis, M. Blat, A. Ambard, R.J. Comstock, et al., The effect of Sn on autoclave corrosion performance and corrosion mechanisms in Zr–Sn–Nb alloys, Acta Mater. 61 (2013) 4200–4214.
[38] H. Okamoto, Fe–Zr (iron–zirconium), J. Phase Equilib. 18 (1997) 316.
[39] H. Okamoto, Nb–Zr (niobium–zirconium), J. Phase Equilib. 13 (1992) 577.
[40] Y.H. Jeong, H.G. Kim, T.H. Kim, Effect of β phase:precipitate and Nb-concentration in matrix on corrosion and oxide characteristics of Zr–*x*Nb alloys, J. Nucl. Mater. 317 (2003) 1–12.
[41] M. Youssef, B. Yildiz, Intrinsic point-defect equilibria in tetragonal $ZrO_2$: density functional theory analysis with finite-temperature effects, Phys. Rev. B. 86 (2012) 144109.
[42] A.S. Foster, V.B. Sulimov, F.L. Gejo, A.L. Shluger, R.M. Nieminen, Structure and electrical levels of point defects in monoclinic zirconia, Phys. Rev. B. 64 (2001), 224108.
[43] J.P. Foster, J. Dougherty, M.G. Burke, J.F. Bates, S. Worcester, Influence of final recrystallization heat treatment on Zircaloy-4 strip corrosion, J. Nucl. Mater. 173 (1990) 164–178.
[44] H.H. Hsu, L.W. Tsay, Fracture properties of hydrided Zircaloy-4 cladding in recrystallization and stress-relief anneal conditions, J. Nucl. Mater. 422 (2012) 116–123.
[45] M. Harada, R. Wakamatsu, The effect of hydrogen on the transition behavior of the corrosion rate of zirconium alloys, J. ASTM Int. 5 (2008) 384–402.
[46] N.A.P. Kiran Kumar, J.A. Szpunar, EBSD studies on microstructure and crystallographic orientation of δ-hydrides in Zircaloy-4, Zr-1% Nb and Zr-2. 5% Nb, Mater. Sci. Engi. A. 528 (2011) 6366–6374.
[47] K. Linga Murty, I. Charit, Texture development and anisotropic deformation of zircaloys, Prog. Nucl. Energy 48 (2006) 325–359.
[48] M.P. Puls, Review of the thermodynamic basis for models of delayed hydride cracking rate in zirconium alloys, J. Nucl. Mater. 393 (2009) 350–367.
[49] Z.N. Yang, F.C. Liu, F.C. Zhang, Z.G. Yan, Y.Y. Xiao, Microstructural evolution and mechanical properties in Zr705 during the rolling process, Mater. Sci. Engi. A. 544 (2012) 54–58.
[50] L. Saintoyant, L. Legras, Y. Bréchet, Effect of an applied stress on the recrystallization mechanisms of a zirconium alloy, Scr. Mater. 64 (2011) 418–421.
[51] H.S. Hong, S.J. Kim, K.S. Lee, Effects of alloying elements on the tensile properties and oxidation behavior of modified Zircaloy-4 in 360 °C water, J. Nucl. Mater. 238l (1996) 211–217.